European Journal of Mechanics / A Solids 74 (2019) 66–80

Contents lists available at ScienceDirect

European Journal of Mechanics / A Solids

journal homepage: www.elsevier.com/locate/ejmsol

Creep-fatigue and cyclically enhanced creep mechanisms in aluminium based metal matrix composites

Dario Giugliano[a], Daniele Barbera[b], Haofeng Chen[a,*], Nak-Kyun Cho[a], Yinghua Liu[c]

[a] Department of Mechanical & Aerospace Engineering, University of Strathclyde, Glasgow, G1 1XJ, UK
[b] School of Engineering, University of Glasgow, Glasgow, G12 8QQ, UK
[c] Department of Engineering Mechanics, Tsinghua University, Beijing, 100084, China

ARTICLE INFO

Keywords:
Linear Matching Method (LMM)
Cyclic plasticity
Low cycle fatigue (LCF)
Creep-fatigue interaction
Metal Matrix Composite (MMC)

ABSTRACT

An aluminium (Al, 2024T3) matrix composite reinforced with continuous alumina (Al_2O_3) fibres is investigated under tensile off-axis constant macro stress and thermal cyclic loading. The micromechanical approach to modelling and three different fibre cross-section geometries have been employed. The effect of creep is included by considering three dwell times at the peak temperature of the thermal loading history. The presence of the hold time gives rise to different sources of failure such as cyclic enhanced creep and creep ratchetting. These failure mechanisms are carefully discussed and assessed. The linear matching method framework has been used for the direct evaluation of the crucial parameters for creep-fatigue crack initiation assessment at the steady cycle. A detailed representation of the steady-state hysteresis loops is provided by using the strain range partitioning and a method for dealing with multiaxiality is reported with regard to the algebraic sign of the Mises-Hencky equivalent stress and strain. All the results obtained have been benchmarked by fully inelastic step-by-step (SBS) analyses. The design of a long fibre metal matrix composite should consider not only the detrimental effect of their dissimilar coefficient of thermal expansion, but also the state of stress at the interface between the matrix and fibre.

1. Introduction

Metal matrix composites (MMCs), are undergoing rapid development to keep up with the requirements of aerospace and automotive industrial sector applications where minimal weight, and increased efficiency are critical factors (Cantor et al., 2003). Predicting composite behaviour under hostile and demanding environments due to the combined action of thermal and mechanical loading, allow for much more effective and reliable use of these complex materials. When a temperature hold time within the cyclic thermal loading is imposed, a combination of thermal fatigue and creep damage occur inside the matrix. Creep produces intergranular cavitation damage that is strongly affected by the hold time's position within the loading cycle. If the creep dwell starts at the pick of the tensile stress, intergranular damage occurs even for short hold times. Fatigue failure instead is a multi-stage process. It begins with the initiation of cracks and with continued cyclic loading the cracks propagate through transgranular paths, with surface striations and wide surface cracks.

In engineering components operating at high temperature, creep lifetime can be significantly reduced when a cyclic mechanical loading is superimposed in the creep regime. Four types of damage's interactions can occur i.e. pure fatigue, transgranular competing, mixed interaction and pure creep (Barbera et al., 2016b), depending on strain range and dwell time (Hales, 1980; Plumbridge, 1987). A better understanding of the micro material scale is necessary to ensure that certain types of failure mechanism do not arise, such as low cycle fatigue (LCF) crack initiation, ratchetting, cyclically enhanced creep or creep ratchetting. This involves the determination of the shakedown limit, ratchet limit, plastic strain range for LCF assessment, and creep cyclic plasticity interaction (Barbera et al., 2016b; Giugliano et al., 2017; Giugliano and Chen, 2016). The schematic representation of the stress-strain material response due to cyclic loading with creep dwell at the tensile peak, as reported in (Barbera et al., 2016b), clarifies the importance of the aforementioned design limits. Indeed when the load level is below the elastic limit, no plastic strain occurs at the first cycle and the subsequent creep stress relaxation does not cause any plasticity during the following unloading and loading phases. Plasticity at the first cycle occurs when the load point is above the elastic limit. Here different scenarios can take place depending upon the load level i.e. the effect of primary and secondary loads, and dwell time. If the load level

* Corresponding author.
E-mail address: haofeng.chen@strath.ac.uk (H. Chen).

https://doi.org/10.1016/j.euromechsol.2018.10.015
Received 26 April 2018; Received in revised form 8 September 2018; Accepted 21 October 2018
Available online 25 October 2018
0997-7538/

is largely below the shakedown limit and the dwell time is short enough, the stress relaxation during the subsequent creep hold times is not significant; hence no plastic strain occurs during the subsequent cycles. The steady-state response is similar to shakedown and the accumulated creep damage is identical to the monotonic load case. Instead for a higher load level in the shakedown zone but close to the shakedown limit, creep enhanced plasticity can occur which lead to either cyclically enhanced creep or creep ratchetting (EDF Energy, 2014). Two scenarios are possible when cyclically enhanced creep occur depending upon the magnitude of the primary and secondary loads. For both cases, a steady-state closed loop response appears either with only creep strain in loading or with both plastic strain and creep strain in loading. As a closed loop is expected, the inelastic strain in loading is compensated by the reverse plasticity in unloading. Compared to the monotonic load, more severe creep-fatigue damage arises. When the inelastic strain in loading is not compensated by the plastic strain in unloading, a mechanism known as creep ratchetting is expected (Chen et al., 2014). Ratchetting is a cyclic phenomenon, which result in the progressive accumulation of plastic strain. From Bree (1967), it is known that for general thermomechanical cyclic loading without hold time, if the structure operates in a region of strict or global shakedown no inelastic strain accumulation occurs. This statement, as discussed previously, becomes imprecise when stress relaxation due to creep dwell arises. Indeed, if within the shakedown zone, particular conditions in terms of load level and hold time are satisfied, either cyclically enhanced creep or creep ratchetting occurs.

The effects of pure thermal fatigue with constant off-axis mechanical load (Chen and Ponter, 2005; Giugliano et al., 2017; Giugliano and Chen, 2016; Jansson et al., 1994; Jansson and Leckie, 1992; Ponter and Leckie, 1998a, b) and thermo-mechanical fatigue (TMF) with hold time (Barbera et al., 2016a; Bettge et al., 2007; Halford et al., 2000; Hertz-Clemens et al., 2002; Mirdamadi and Johnson, 1996; Mondali et al., 2005; Nicholas et al., 1996; Rutecka et al., 2011) on MMCs have been under the attention of the authors over the last five years. Also, experimental observation on the ratchetting behaviour of metal matrix composites reinforced by continuous fibre, particle and whisker are reported in (Zhang et al., 1990), (Daehn et al., 1991), and (Jansson and Leckie, 1991) in the case of loading condition with a constant stress and cyclic thermal loading, respectively. More recently, a detailed experimental investigation on the SiC_P/6061Al alloy particle reinforced metal matrix composites (PRMMC) at room and high temperature have been carried out by (Kang, 2006). It has been shown that (1) the SiC_P/6061Al alloy composites presents a ratchetting similar to that of 6061-T6 aluminium alloy matrix in a macroscopic sense; (2) the addition of SiC ceramic particle improves the resistance of the composites to ratchetting deformation remarkably, and the ratchetting strain produced in the composites decreases with the increasing volume fraction of particles; (3) the ratchetting is time-dependent at room and high temperatures (573 K). Starting from the experimental observation (Kang, 2006; Kang et al., 2007; Shao et al., 2009; Shao et al., 2010), carried out reasonable finite element simulations to investigate the time-independent and time-dependent ratchetting of SiC_P/6061Al alloy composites at room and high temperatures, by employing newly developed cyclic elasto-plastic and visco-plastic constitutive models (Kang, 2004). Furthermore (Guo et al., 2007), and (Kang, 2008) provided numerical simulations to the uniaxial ratchetting of SiC_P/6061Al composites by using a three-dimensional multi-particle unit cell with regular particle arrangement. Due to some limitations i.e. mesh density and computational efficiency, of investigating the ratchetting behaviour by means of FEM simulations and 3D RVEs, a cyclic constitutive model in a macroscopic sense was proposed by (Guo et al., 2011). The capability of the proposed model to predict the uniaxial ratchetting of the composites is verified by comparing the predicted results with the experimental ones of the SiC_P/6061Al composites with different volume fractions of particles and at room temperature. Also, based on the generalized incrementally affine linearization method (Doghri et al., 2010) and the extended version of Mori-Tanaka homogenization model (Guo et al., 2011), a new cyclic visco-plastic meso-mechanical constitutive model was proposed in (Guo et al., 2013) to predict the time-dependent ratchetting of SiC_P/6061Al composites presented under the stress controlled cyclic loading conditions at various stress rates and with certain peak stress holds.

The aim of this work is to investigate the impact of three different fibre cross-section geometries i.e. circular cross-section, elliptical cross-section and square cross-section on the creep-fatigue interaction behaviour of continuous fibre reinforced aluminium matrix composites (CFAMCs). For the loading conditions investigated, the stress state at the matrix-fibre's interface, gives rise to a new ratchetting mechanism which affects the cyclic stress-strain hysteresis loop of CFAMCs. Indeed, by superimposing a cyclic thermal load with dwell time over an off-axis constant macro stress, a scenario where mechanical and thermal stresses at the matrix-fibre's interface act in the opposite direction can occur. In this situation, the effect of both stress relaxation and residual stress field can lead the structure to experience creep ratchetting with a total open hysteresis loop (TOL). This work, will explore the damaging effect of this new mechanism which has been neglected in (Barbera et al., 2016a, b). A great number of numerical simulations are required to study different geometries, with each being subjected to a variety of loading conditions and dwell times. For this reason the traditional Abaqus (2013) incremental finite element approach is not a viable option due to the large computational cost. In order to perform an accurate and efficient analysis the Linear Matching Method (LMM) is used in this work, which has been demonstrated to be capable of providing solutions for different classes of problems (Chen, 2010; Chen et al., 2014; Chen and Ponter, 2010; Giugliano et al., 2017; Giugliano and Chen, 2016; Gorash and Chen, 2013; Xuanchen Zhu et al., 2017). Recently the extended LMM Direct Steady Cyclic Analysis (eDSCA) has been adopted by the authors to perform a preliminary study on the creep and fatigue response of a MMCs unit cell (Barbera et al., 2016a), further demonstrating the method's applicability. Although the numerical results presented require extensive experimental verifications before they can be generally adopted, the experimental observations reported in (Kang, 2006) on PRMMCs can be taken into account to verify the reasonability of the numerical simulations of this study.

2. Numerical method

The main idea of investigating the creep-fatigue behaviour of MMCs by means of the LMM relies upon its capabilities to predict the anisotropic composite behaviour by assigning the isotropic constitutive models to each of the composite constituent i.e. matrix and fibre, if the micromechanical approach to modelling is used.

In order to calculate the steady-state cycle response of a structure subjected to an arbitrary cyclic load history, a numerical procedure based on the minimization process of $I(\dot{\varepsilon}_{ij}^{c}) = \sum_{l=1}^{L} I^{l}$ has been developed (Chen et al., 2014; Chen and Ponter, 2006) and further tested (Barbera et al., 2016a; Gorash and Chen, 2013). This function is related to a class of kinematic admissible strain rate $\dot{\varepsilon}_{ij}^{c}$, defined for a L total number of loading instances. An incremental form has been proposed for the minimization function as follow:

$$I^{l}(\Delta\varepsilon_{ij}^{l}) = \int_{V} \left\{ \sigma_{ij}^{l}\Delta\varepsilon_{ij}^{l} - \left[\hat{\sigma}_{ij}^{l}(t_l) + \rho_{ij}^{l}(t_l) \right] \Delta\varepsilon_{ij}^{l} \right\} dV \tag{1}$$

Where σ_{ij}^{l} is the cyclic stress calculated at load instance "l", $\Delta\varepsilon_{ij}^{l}$ is the inelastic strain increment, and $\hat{\sigma}_{ij}^{l}(t_l)$ is the linear elastic stress associated to the cyclic history considering cyclic and constant loading and $\rho_{ij}^{l}(t_l)$ is the residual stress at each load instance. This residual stress is calculated by the sum of the constant part of the changing residual stress $\bar{\rho}_{ij}$ and the summation of all the previous changing residual stress field increments $\Delta\rho_{ij}(t_l)$. This incremental formulation allows the strain rate history $\dot{\varepsilon}_{ij}^{c}$ to be replaced with a sequence of increments of strain $\Delta\varepsilon_{ij}^{l}$, which occur during the load cycle at each time t_l. The eDSCA is

capable of calculating, by iterative mean, the inelastic strain increment $\Delta\varepsilon_{ij}^{l}$, which minimize the function shown in equation (1). A total of K sub-cycles are requested to reach the convergence. Within each k sub-cycle a total of L load increments need to be performed. The residual stress field and inelastic strain increment associated to each load instance l are obtained. At each increment the residual stress and inelastic strain are calculated by the elastic stress and the previous accumulated residual stresses. When the load instance does not contain a creep dwell, the plastic strain increment $\Delta\varepsilon_{ij,k+1}(t_l)'$ can be calculated by:

$$\Delta\varepsilon_{ij,k+1}(t_l)' = \frac{1}{2\bar{\mu}(t_l)}[\hat{\sigma}_{ij}(t_l) + \rho_{ij,k+1}(t_{l-1}) + \Delta\rho_{ij,k+1}(t_l)]' \tag{2}$$

where notation (') refers to the deviator component of stresses and $\bar{\mu}$ is the iterative shear modulus (Chen et al., 2014), $\hat{\sigma}_{ij}$ is the associated elastic solution, $\rho_{ij,k+1}(t_{l-1})$ is the prior changing residual stress history and $\Delta\rho_{ij,k+1}(t_l)$ is the residual stress associated to the inelastic strain increment. If required, the calculated plastic strain is used to iteratively change the yield stress in the upcoming $k+1$ sub-cycle, considering the Ramberg-Osgood (RO) (Skelton et al., 1997) material response. The Ramberg-Osgood model is based on the interpolation of cyclic data at different strain range at the steady state (saturated cycle). The combination of all these points' forms the well-known “locus of the tips” (Hales et al., 2002). This approach allows considering the stabilised loop, at different strain range, for cyclic hardening or softening materials, however does not consider the evolution of the cyclic response of the structures that is considered negligible.

In load cases where creep is present, the equivalent creep strain increment $\Delta\bar{\varepsilon}^{c}$ is calculated by the following equation for the associated dwell time Δt using the Norton-Bailey relation:

$$\Delta\bar{\varepsilon}^{c} = \frac{B(n-1)\Delta t^{m+1}(\bar{\sigma}_s - \bar{\sigma}_c)}{\left(\frac{1}{\bar{\sigma}_c^{n-1}} - \frac{1}{\bar{\sigma}_s^{n-1}}\right)(m+1)} \tag{3}$$

where B,m and n are the creep constants of the material. $\bar{\sigma}_c$ represents the creep flow stress, which is the sum of the start-of-dwell stress $\bar{\sigma}_s$ and the residual stress $\Delta\rho_{ij}^{c}$ caused by the dwell period. The creep flow stress is then determined by accurately evaluating the creep strain rate $\dot{\bar{\varepsilon}}^{F}$ at the end of the dwell time:

$$\bar{\sigma}_c = \left(\frac{\dot{\bar{\varepsilon}}^{F}}{B\Delta t^{m}}\right)^{\frac{1}{n}}$$
$$\dot{\bar{\varepsilon}}^{F} = \frac{\Delta\bar{\varepsilon}^{c}}{\Delta t}\frac{(m+1)}{(n-1)}\frac{\bar{\sigma}_c^{n}}{(\bar{\sigma}_s - \bar{\sigma}_c)}\left(\frac{1}{\bar{\sigma}_c^{n-1}} - \frac{1}{\bar{\sigma}_s^{n-1}}\right) \tag{4}$$

The remaining part of the procedure calculates the residual stress at each increment through the solution of linear problems. The residual stress field and the iterative shear modulus obtained are updated for the next cycle $k+1$ for each load instance t_l by adopting the linear matching equation;

$$\bar{\mu}_{k+1}(x, t_l) = \bar{\mu}_k(x, t_l)\frac{\sigma_y^{R}(x, t_l)_k}{\bar{\sigma}\left(\hat{\sigma}_{ij}(x, t_l) + \rho_{ij}^{r}(x, t_l)_k\right)} \tag{5}$$

where $\bar{\mu}_k(x, t_l)$ is the iterative shear modulus at the sub-cycle k for lth load instance. $\sigma_y^{R}(x, t_l)_k$ is the iterative yield stress for RO material model or yield stress for the Elastic Perfectly Plastic material model at load instance t_l. The yield stress $\sigma_y^{R}(x, t_l)_k$ will be replaced by creep flow stress $\bar{\sigma}_c$ if creep relaxation occurs at the load instance. $\rho_{ij}^{r}(x, t_l)_k$ is the sum of the constant residual stress field and all the previous changing residual stresses at different load instances. This procedure is capable of characterizing the whole steady-state cycle calculating both plastic and creep response and considering their combined effects. Once the entire numerical process is converged the creep fatigue endurance can be evaluated. The required key parameters for the assessment can be accurately calculated from the stabilised hysteresis loop by adopting the procedure depicted in Fig. 1 and it is based on the procedure developed by (Wada et al., 1997). The fatigue and creep damage are accounted separately by the evaluating the total strain range, the stress at the start of creep dwell, the stress drop, the average creep rupture stress and creep strain accumulated during the dwell. In addition, compressive creep dwells are identified and neglected to avoid introducing overly conservative assessments.

3. Problem description and finite element models

The modelling strategy employed for this study, relies on the micromechanical approach where, in the presence of material non-linearity, the anisotropic composite behaviour is predicted by using constitutive models for the isotropic constituent materials (Aboudi et al., 2012). The same modelling strategy has been used in our previous paper where the authors investigated the effect of fibre cross-section geometry on the cyclic plastic behaviour of fibre reinforced MMCs (Giugliano et al., 2017).

Here, three geometries have been considered: circular cross-section, elliptical cross-section and square cross-section, all arranged in a square packing pattern (Fig. 2a). Plane strain assumption is suitable for such application as the dimension in the direction of the fibre, referred to as direction z, is much larger than the other two. Therefore, strain components ε_{xz}, ε_{yz} and ε_{zz} are equal to zero at any time. Due to the symmetry, only a quarter of the unit cells have been considered (Fig. 3). Therefore, symmetry conditions along with plane conditions, applied by Abaqus constraint equations, have been imposed (Fig. 2b). The meshes are composed respectively by 3507, 3692 and 2326 8-node biquadratic plane strain quadrilateral elements, with a reduced integration scheme. This modelling strategy is suggested in (Chen and Hachemi, 2014), when a stress approach is considered on the local scale. Indeed, for stress approach, beside the uniform stress imposed on the boundary, one degree of freedom of the boundary is coupled in order to maintain the periodic deformation. Despite periodic boundary conditions are more realistic, both stress approach and strain approach provide a consistent deformation of the boundary (Chen and Hachemi, 2014).

An aluminium matrix (Al, 2024T3) reinforced with 30% of alumina (Al_2O_3) is considered. A viscoplastic model without cyclic hardening simulates the former while a perfectly elastic model simulates the latter. The fibre has a Young's modulus (E) of 370 GPa, a Poisson's ratio (ν) of 0.26, a coefficient of thermal expansion (CTE) of $8 \times 10^{-6}\,°C^{-1}$ and a ultimate tensile strength (UTS) 5000 MPa while the matrix has a Young's modulus of 73 GPa, a Poisson's ratio of 0.33, a coefficient of thermal expansion of $23 \times 10^{-6}\,°C^{-1}$ and the temperature dependent yield stress is reported in Table 1.

Due to the temperature considered, it is relevant to evaluate the creep strain only for the aluminium matrix. The creep constitutive equation adopted is the Norton-Bailey law:

$$\dot{\varepsilon}^{cr} = A{\cdot}\sigma^{n}{\cdot}t^{m} \tag{6}$$

where n is the stress exponent, m is the time exponent for the primary creep stage and A $[MPa^{-n} \times h^{-(m+1)}]$ is the power law multiplier, the tensile creep data are taken from (Maximov et al., 2014) and reported in Table 2.

In order to explore the effect of different fibre cross-section geometry on the creep-fatigue response, shakedown boundaries for the models in Fig. 3, which are related to the previous study are considered and shown in Fig. 4a. The axes are expressed in non-dimensional variables $\sigma_p/\sigma_y^{(25)}$ and $\Delta\theta/\Delta\theta_0$ where $\sigma_y^{(25)} = 371MPa$ is the yield stress at 25 °C while $\Delta\theta_0 = 50°C$ is the reference temperature load range. A uniaxial macro-stress $\sigma_p = 371MPa$ is applied in a direction perpendicular to opposing faces of the unit cells and is maintained constant while a cyclic temperature field with hold time Δt is applied uniformly over the unit cells, with a varying range from $0°C$ to $\Delta\theta_0$ (Fig. 4b). Three load points are investigated and shown in Fig. 4a i.e. A_1 (0, 3.5), A_2 (0.25, 3.5) and A_3 (0.5, 3.5), which represent shakedown for both the

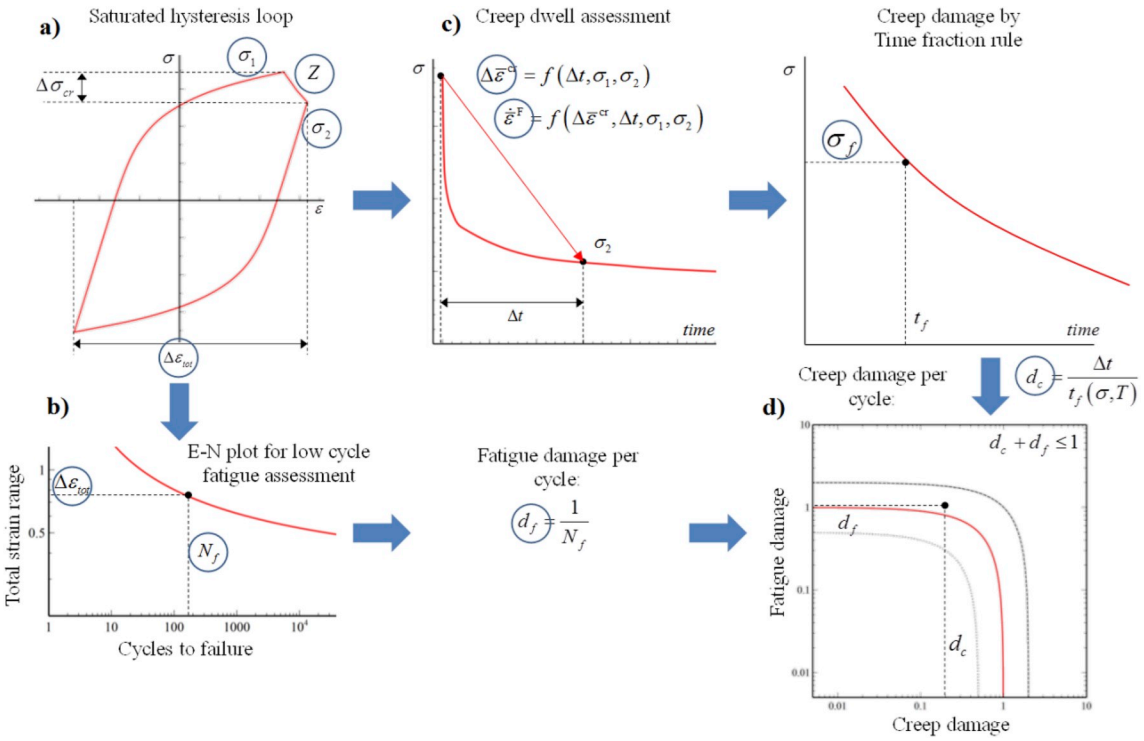

Fig. 1. Creep fatigue assessment procedure adopted for crack initiation assessment. a) The saturated hysteresis loop is characterized by the eDSCA, b) the total strain range is used to estimate the number of cycle to failure due to fatigue and the associated damage per cycle, c) the creep dwell is assessed determining the damage per cycle, d) the total damage is calculated.

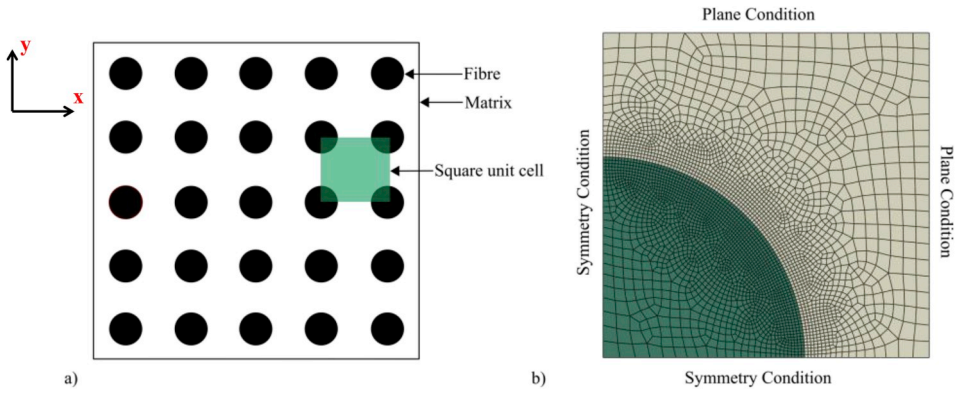

Fig. 2. a) Square packing pattern, b) Quarter of the unit cell with applied boundary conditions.

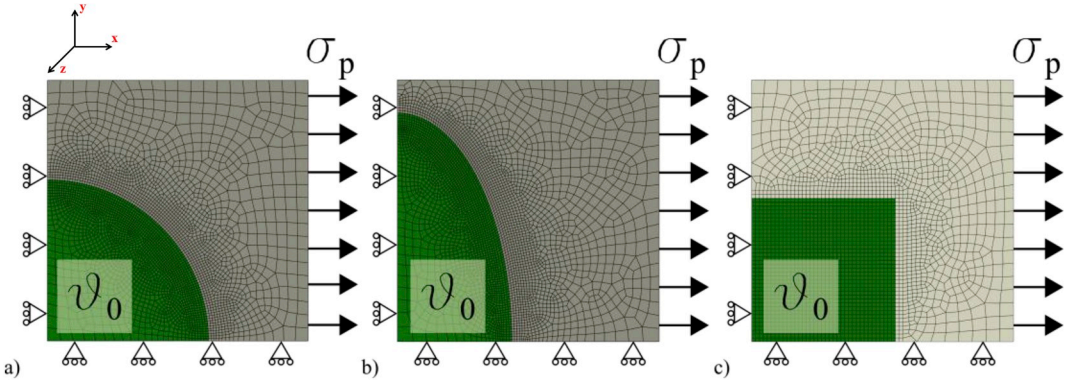

Fig. 3. Finite element models for the a) circular cross-section, b) elliptical cross-section and c) square cross-section.

Table 1
Temperature dependent yield stress for 2024T3 aluminium alloy.

	25 °C	150 °C	175 °C	200 °C
σ_y[MPa]	371	351	322	315

Table 2
Creep parameters A, n and m for 2024T3 aluminium alloy.

	150 °C	175 °C	200 °C
A	$0.763 \cdot 10^{-12}$	$3.461 \cdot 10^{-12}$	$4.079 \cdot 10^{-12}$
n	3.246	3.299	3.395
m	− 0.303	− 0.573	− 0.535

circular cross-section and the elliptical cross-section and reverse plasticity for the square cross-section when the applied cyclic loading condition does not have the hold time Δt (Figure.3 of (Giugliano et al., 2017)). By introducing a high temperature dwell time as shown in Fig. 4b, creep enhanced plasticity may occur (Barbera et al., 2016a) as discussed in section 1. In order to explore the influence of the dwell time on the steady-state behaviour of MMCs, each load point is investigated for three different dwell times i.e. 1 h, 10 h, 100 h referred to as D1, D10, D100 within the paper.

When the authors performed this study, no low cycle fatigue data for Al2024T3 was available at high temperature, this is often the case and in most cases do not cover all the operating conditions required for an assessment procedure. For this reason a robust and efficient method was created by (Coffin Jr, 1954; Manson, 1954, 1968; Muralidharan and Manson, 1988) and further modified. The key concept of these methods is to estimate the fatigue life from common tensile test. If creep has to be considered, creep rupture test are also used. Such approach is based on the possibility to separate the LCF plot into two strain components the elastic and plastic one. Using the following relationship for the elastic $\Delta\varepsilon_{el}$ and plastic strain $\Delta\varepsilon_{pl}$ range:

$$\Delta\varepsilon_{el} N_f^{\alpha_1} = C_1 \tag{7}$$

$$\Delta\varepsilon_{pl} N_f^{\alpha_2} = C_2 \tag{8}$$

where α_1 and α_2 are material properties related to the slopes, and C_1 and C_2 are related to the fatigue ductility. By combining equations (7) and (8) the Coffin-Manson relationship is derived, which relates the total strain range $\Delta\varepsilon_{tot}$ with the number of cycles to fail N_f.

$$\frac{\Delta\varepsilon_{tot}}{2} = \frac{\sigma_f'}{E}\cdot(2N_f)^b + \varepsilon_f'\cdot(2N_f)^c \tag{9}$$

The right hand part of (9) represents respectively the elastic strain range and the plastic strain range, where the coefficient σ_f' is related to the material fatigue strength, instead ε_f' is the material fatigue ductility strength. Manson and others developed and modified equation (9) obtaining the "Universal Slope Method (USM)" (Manson, 1965; Muralidharan and Manson, 1988) assuming that the slopes coefficient b and c are constants. Furthermore, the equations for σ_f' and ε_f' have been developed and proposed by Manson in his work (Manson, 1965) defining the total strain range as follow:

$$\frac{\Delta\varepsilon_{tot}}{2} = \frac{\sigma_f'}{E}\cdot(2N_f)^b + \varepsilon_f'\cdot(2N_f)^c \tag{10}$$

The fatigue strength coefficients and the fatigue ductility are calculated using the following equations:

$$\sigma_f' = E\cdot 0.623\cdot\left(\frac{S_u}{E}\right)^{0.832}$$
$$\varepsilon_f' = 0.0196\cdot\varepsilon_f^{0.155}\cdot\left(\frac{S_u}{E}\right)^{-0.53} \tag{11}$$

where S_u is the ultimate stress and ε_f is the strain to failure at the desired temperature both obtained by tensile tests. Cyclic strength and ductility are determined by this empirical equation system (11) with specific multipliers and exponents calibrated on vast number of tests. Instead the exponents of equation (10) are assumed constant b = −0.09 and c = −0.56. The ultimate strength S_u is selected for the appropriate temperature and hold time, and it is shown in Table 3. Only recently an experimental work on monotonic and low cycle fatigue behaviour of Al2024T3 at room and high temperature has been published (Karakaş and Szusta, 2015). A comparison between the adopted modified universal slope method and experimental data is presented in Fig. 5, showing a good and slightly conservative approximation.

Table 3
Temperature dependent tensile strength for 2024T3 aluminium alloy.

Su[MPa]	150 °C	175 °C	200 °C
0.1 h	550	436	460
1 h	415	395	370
100 h	435	370	305
1000 h	400	330	260

In order to evaluate the creep rupture time the stress dependent reversed power-law is used:

$$t^* = B\cdot\sigma^{-k} \tag{12}$$

where B = 1.93642E+017 and k = 6.2252 are creep rupture material parameters estimated by fitting the experimental creep rupture data available for the required temperature (175 °C for the creep-fatigue assessment). When the rupture time is determined the time fraction rule

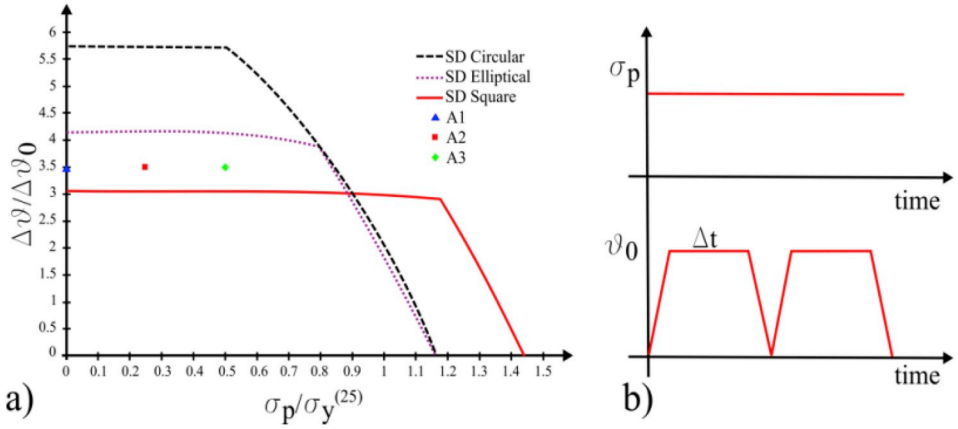

Fig. 4. a) Shakedown limit boundaries for the three cross-section geometries analysed under constant mechanical load and cyclic thermal loading without dwell time, b) load history applied with dwell time related to the point A1, A2, and A3.

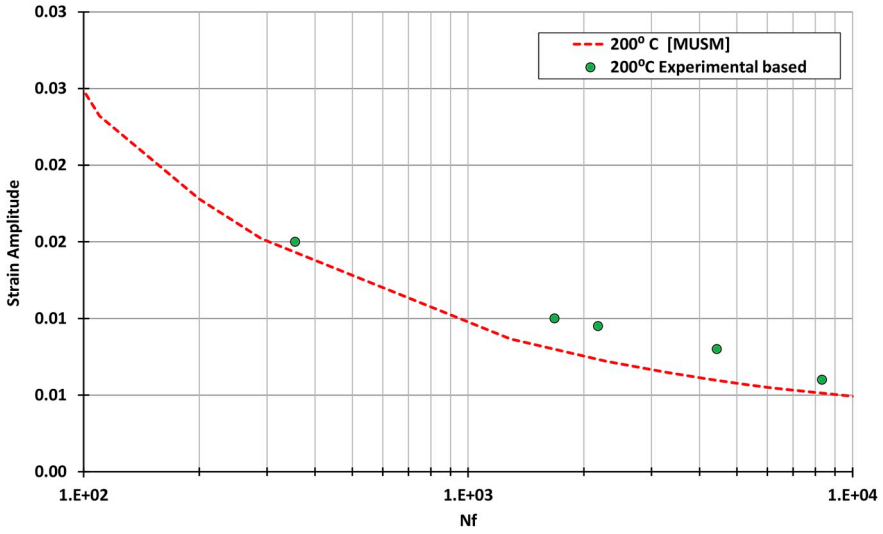

Fig. 5. Comparison between Modified Universal Slope Method and experimental results (Karakaş and Szusta, 2015).

is adopted to calculate the total creep damage. Once both the damages due to fatigue ω_f and creep ω_c are calculated separately, a linear damage interaction $\omega_f + \omega_c \leq 1$ is adopted to calculate the total number of cycle to fail and the total damage as well.

4. Modified strain range partitioning

Strain range partitioning is a method for treating creep-fatigue interaction at elevated temperature where stress mutiaxiality is involved. A full description of the strain range partitioning procedure is reported in (Manson and Halford, 1976). Here, as suggested in (Manson and Halford, 1976), further studies have been undertaken in order to understand the effect of anisotropy which arises in composite structures, non-proportional loading and high temperature on the creep-fatigue interaction behaviour. Also, a modification of the method has been proposed aimed at providing information on both the transition and steady-state behaviour. This procedure relies upon the comparison between the ratchetting strain computed between two subsequent hysteresis loops and the ratchetting strain computed within the hysteresis loop itself by using the strain range partitioning approach. A detailed description of the procedure which is based on incremental FEA is reported in the following subsections. Comparison with the LMM procedure is also reported in order to show the capability of the direct methods to provide feasible and computational inexpensive solutions to assess the steady-state cyclic response.

4.1. Evaluation of the equivalent stress and strain

The first step is to compute the strain increments at each time instant within the cycle. We refer to 8 schematic hysteresis loops that, as will be seen in section 5, characterise the material response under the assigned loading history for both procedures.

Fig. 6a-b-c-d show the schematic steady state hysteresis loops related to the step-by-step (SBS) procedure while Fig. 6e-f-g-h show the hysteresis loops related to the Linear Matching Method (LMM) procedure. The four loops depicted in Fig. 6a-b-e-f are referred to as total open loops (TOL) whereas the four loops depicted in Fig. 6c-d-g-h are referred to as reverse open loops (ROL) if the points P1 and P6 are different while for P1 = P6 they are referred to as reverse closed loop (RCL). For both procedures the elastic strain increment in loading is computed between points P1-P2, the plastic strain increment in loading between points P2-P3, the creep strain increment between points P3-P4, the elastic strain increment in unloading between points P4-P5, and the plastic strain increment in unloading between points P5-P6. It is noted that point P3 is present in the loops only when plastic strain in loading occurs. Hence for the loops in Fig. 6a-c-e-g the starting point of the creep phase is P2 and the creep strain increment is computed between points P2-P4.

The main difference between the SBS procedure and the LMM procedure is in computing the load points P2 and P5 within the steady state hysteresis loop when plastic strain occurs in both loading and unloading. Indeed, as the yield stress varies with the temperature (Table 1), the yield surface becomes smaller during the loading phase as the temperature increases while during the unloading phase the yield stress increases as the temperature decreases. Thus, the point P2 where the accumulation of plastic strain starts in loading for the loops in Fig. 6b–d related to the SBS procedure has an equivalent von Mises stress higher than the point P3 where the stress level is equal the yield stress at the peak temperature within the thermal loading history. For the LMM procedure the point P2 depicted in Fig. 6f–h starts always at the same stress level as P3 which is equal to the yield stress at the peak temperature within the thermal loading history. Same conclusion can be drawn for the point P5 where the accumulation of plastic strain starts in unloading. As the yield surface increase during the unloading phase for the SBS procedure, point P5 has an equivalent von Mises stress lower that the yield stress at room temperature (Fig. 6b–d) while for the LMM procedure point P5 depicted in Fig. 6f–h starts always from the same stress level as P6.

Let's assume that the effect of the three principal components of stress and strain is characterized by single parameters according to the equations:

$$\bar{\sigma}_e = \frac{1}{\sqrt{2}}\sqrt{(\sigma_1-\sigma_2)^2-(\sigma_2-\sigma_3)^2-(\sigma_3-\sigma_1)^2} \tag{13}$$

$$\bar{\varepsilon}_{el} = \frac{1}{(1+\nu)\sqrt{2}}\sqrt{(\varepsilon_1^{el}-\varepsilon_2^{el})^2+(\varepsilon_2^{el}-\varepsilon_3^{el})^2+(\varepsilon_3^{el}-\varepsilon_1^{el})^2} \tag{14}$$

$$\bar{\varepsilon}_{in} = \frac{\sqrt{2}}{3}\sqrt{(\varepsilon_1^{in}-\varepsilon_2^{in})^2+(\varepsilon_2^{in}-\varepsilon_3^{in})^2+(\varepsilon_3^{in}-\varepsilon_1^{in})^2} \tag{15}$$

wherein $\bar{\sigma}_e$ is the equivalent stress at a generic cycle, time step, and time increment, $\bar{\varepsilon}_{el}$ is the equivalent elastic strain and $\bar{\varepsilon}_{in}$ is the equivalent strain for the inelastic components where "*in*" can be "*pl*" (plastic), or "*cr*" (creep). For both stress and strain the subscript "*1*", "*2*" and "*3*" stands for maximum principal component, medium principal component and minimum principal component, respectively.

Upon defining the effective Young's Modulus as $E_{eff} = \frac{3E}{2(1+\nu)}$ (EDF Energy, 2014) the six load points of the stabilised hysteresis loops by means of the SBS procedure are computed using equations (13)–(15)

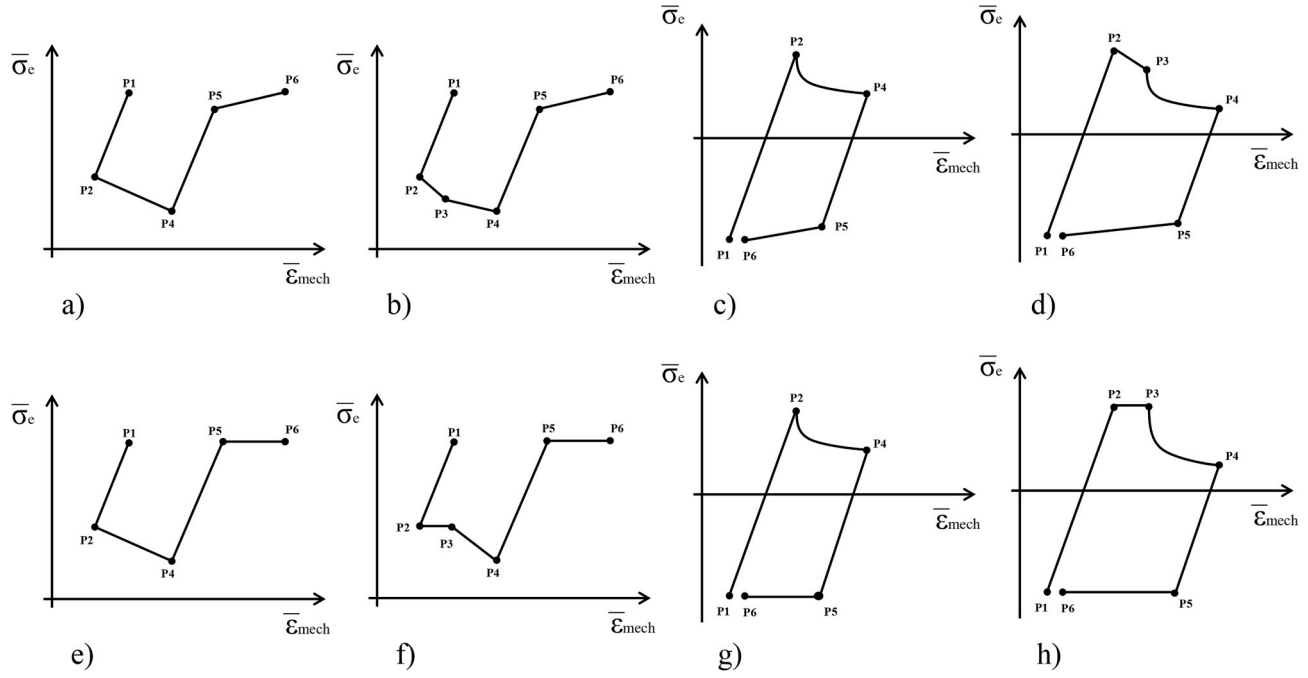

Fig. 6. Schematic steady state hysteresis loops for both SBS approach and LMM approach.

Table 4
Strain increments at different load points of the stabilised hysteresis loop.

	P1	P2	P3	P4	P5	P6
Elastic strain	$\bar{\varepsilon}_{elP1}$	$\Delta\bar{\varepsilon}_{elP2}$	$\Delta\bar{\varepsilon}_{elP3}$	$\Delta\bar{\varepsilon}_{elP4}$	$\Delta\bar{\varepsilon}_{elP5}$	$\Delta\bar{\varepsilon}_{elP6}$
Plastic strain	n/a	n/a	$\Delta\bar{\varepsilon}_{plP3}$	n/a	n/a	$\Delta\bar{\varepsilon}_{plP6}$
Creep strain	n/a	n/a	n/a	$\Delta\bar{\varepsilon}_{crP4}$	n/a	n/a
Total inelastic strain	$\bar{\varepsilon}_{inP1}$	n/a	n/a	n/a	n/a	n/a

and the strain increments for each load point within the loop are reported in Table 4. It is worth noting that the load point P1 is the last load point of the loop that precedes the stabilised loop. Hence $\bar{\varepsilon}_{inP1}$ is the accumulated inelastic strain from the first cycle to the cycle that precedes the stabilised cycle. A similar approach is used by the LMM where all the strain ranges and equivalent stresses are directly calculated for the stabilised hysteresis loop and stored in Abaqus state variables SDV (Abaqus, 2013).

4.2. Evaluation of the algebraic sign of the equivalent stress and strain

As seen in section 4.1, all the equivalent values are evaluated in magnitude. For practical design situations for which life prediction methods are intended to be used, often involve stresses in more than one direction. Thus, the eventual usage of the strain-range partitioning method requires the entire stabilised stress-strain hysteresis loops to be known. From the values of equivalent stress and strain at each point in the cycle, it then becomes possible to construct an equivalent hysteresis loop wherein at each instant of time the stress is the equivalent stress and the strain is the equivalent strain. However, before this can be done an algebraic sign to indicate tension or compression status must be assigned to both magnitudes of equivalent stress and strain (Manson and Halford, 1976). The method proposed comprises of two stages. The first stage is aimed at evaluating the algebraic sign of the equivalent stress and strain within the first hysteresis loop. In particular, at each instant of time the equivalent stress and strain will be computed according to (13), (14), and (15) but the algebraic sign of $\bar{\sigma}_e$ and $\bar{\varepsilon}_{in}$ will be the same as the one of the dominant stress component i.e. the sign of the largest component between σ_1 and σ_3 for the stress and the sign of the largest component between ε_1^{in} and ε_3^{in} for the starin. Table 5 shows the sign of the first cycle related to the reference transition hysteresis loops depicted in Fig. 7. The circular, elliptical and square cross sections are referred to as C11, C21, and S11 respectively within Table 5 where M0 stands for mechanical load $\sigma_p = 0$, M025 stands for $\sigma_p = 0.25 \times \sigma_y^{(25)}$, and M05 stands for $\sigma_p = 0.5 \times \sigma_y^{(25)}$. As previously mentioned, D1 stands for 1 h of dwell time and D100 stands for 100 h of dwell period. Also, L, C, and U stand for end of loading phase, end of creep phase, and end of unloading phase respectively.

Table 5
Sign of von Mises stresses at the first cycle for the reference transition hysteresis loops in Fig. 7.

	$\bar{\sigma}_e$		σ_1	σ_3	*Sign*
C11-M0-D1	L	322	56.0598	−313.566	–
	C	254.933	46.2544	−249.238	–
	U	92.2509	78.5282	−27.7436	+
C11-M025-D100	L	322	159.936	−183.87	–
	C	179.248	128.372	−63.2164	+
	U	312.495	300.479	−40.3999	+
C11-M05-D100	L	322	261.845	−78.3248	+
	C	250.321	264.915	−22.5227	+
	U	371	361.761	−16.3537	+
C21-M0-D100	L	322	232.372	−106.614	+
	C	165.525	180.501	−2.45734	+
	U	371	163.554	−228.67	–
C21-M025-D100	L	322	145.467	−209.131	–
	C	149.572	88.3183	−70.7236	+
	U	328.142	265.309	−74.3077	+
C21-M05-D100	L	322	191.087	−156.857	+
	C	222.665	197.843	−51.489	+
	U	371	293.351	−134.602	+
S11-M0-D100	L	322	365.054	−2.42783	+
	C	188.02	278.731	61.8641	+
	U	371	168.92	−232.541	–

With regards to the second stage, it is aimed at evaluating the sign of the hysteresis loop from the second cycle to the stabilised cycle. Uppermost, we compute the ratchetting strain per cycle in three steps:

1. At the end of each load cycle, 6 components of the mechanical strain are obtained by subtracting corresponding thermal strain

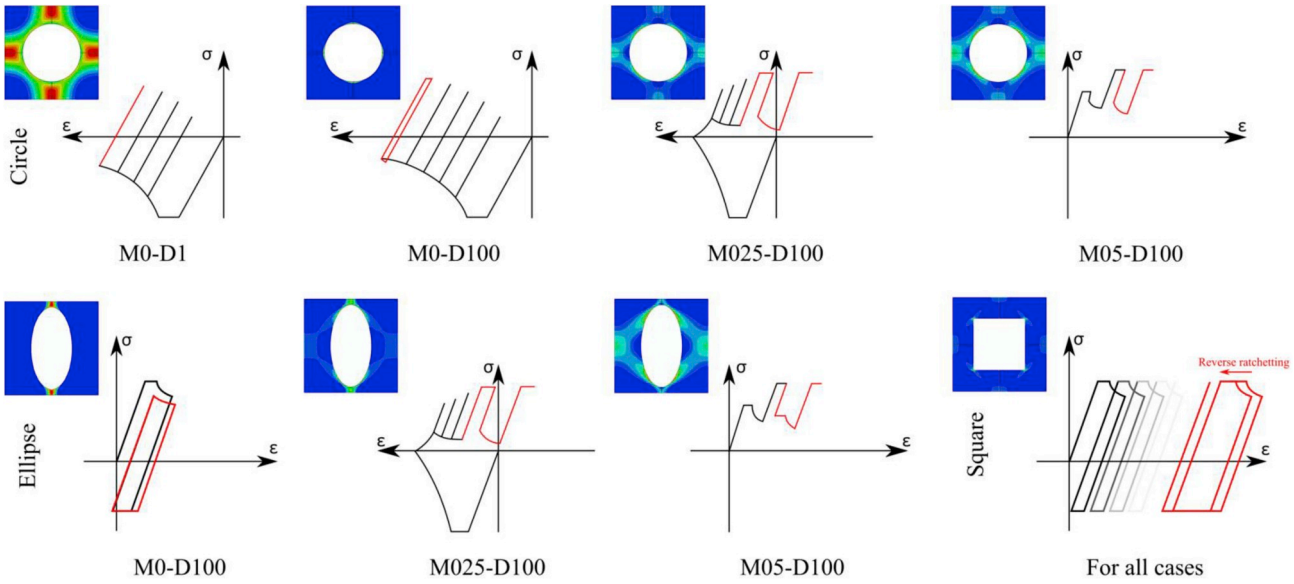

Fig. 7. Schematic transition hysteresis loops for the 3 cross-section studied under the load history in Fig. 4b for different mechanical loads and different dwell times, where the steady state loop is highlighted in RED. (For interpretation of the references to colour in this figure legend, the reader is referred to the Web version of this article.)

components from total strain components. And then 6 components of the ratchetting strain are calculated for each load cycle by the difference in corresponding components of mechanical strain between the end and the beginning of each load cycle;

2. The equivalent ratchetting strain for each load cycle from the 2nd cycle to the stabilised cycle can then be calculated by equation (15) since ratchetting strain is treated as inelastic strain;
3. Taking into account only the final steady state cycle, we compare the equivalent ratchetting stain $\Delta\bar{\varepsilon}_{rtch}$ with the equivalent plastic strain increment in loading $\Delta\bar{\varepsilon}_{pl_{P3}}$, the equivalent creep strain $\Delta\bar{\varepsilon}_{cr_{P4}}$ and the equivalent plastic strain increment in unloading $\Delta\bar{\varepsilon}_{pl_{P6}}$. Three scenarios can occur:

$$\Delta\bar{\varepsilon}_{rtch} \cong \Delta\bar{\varepsilon}_{rtch}^{summ} = \Delta\bar{\varepsilon}_{pl_{P3}} + \Delta\bar{\varepsilon}_{cr_{P4}} + \Delta\bar{\varepsilon}_{pl_{P6}} \rightarrow \text{total open loop (TOL)} \tag{16}$$

$$\Delta\bar{\varepsilon}_{rtch} \cong \Delta\bar{\varepsilon}_{rtch}^{diff} = \Delta\bar{\varepsilon}_{pl_{P3}} + \Delta\bar{\varepsilon}_{cr_{P4}} - \Delta\bar{\varepsilon}_{pl_{P6}} \rightarrow \text{reverse open loop(ROL)} \tag{17}$$

$$\Delta\bar{\varepsilon}_{rtch} \cong 0 \rightarrow \Delta\bar{\varepsilon}_{pl_{P3}} + \Delta\bar{\varepsilon}_{cr_{P4}} \cong \Delta\bar{\varepsilon}_{pl_{P6}} \rightarrow \text{reverse closed loop(RCL)} \tag{18}$$

Upon comparing the ratchetting strain, we can use equations (16) and (17), to evaluate the percentage error as:

$$err\%_{sum} = \frac{|\Delta\bar{\varepsilon}_{rtch} - \Delta\bar{\varepsilon}_{rtch}^{summ}|}{\Delta\bar{\varepsilon}_{rtch}} \times 100 \tag{19}$$

$$err\%_{diff} = \frac{|\Delta\bar{\varepsilon}_{rtch} - \Delta\bar{\varepsilon}_{rtch}^{diff}|}{\Delta\bar{\varepsilon}_{rtch}} \times 100 \tag{20}$$

By computing the percentage error from equations (19) and (20), the stabilised hysteresis loops can be drawn and the 6 load points (5 if no plastic strain in loading occurs i.e. there is no point P3) are univocally determined in terms of both magnitude and sign. Indeed a total open loop (TOL) is considered if $err\%_{sum} < err\%_{diff}$ instead a reverse open loop (ROL) is considered if $err\%_{sum} > err\%_{diff}$. It is worth pointing out that a TOL in this paper is a hysteresis loop where the von Mises stress at each load point is always positive as shown in Fig. 6a-b-e-f. Instead, a ROL can have either the stresses of both the loading and creep phase positive and the stresses of the unloading phase negative as shown in Fig. 6c-d-g-h or vice versa.

5. Application of the concepts to MMCs and discussions

5.1. Transition behaviour

As discussed in section 4, we proposed a variation of the strain range partitioning in order to evaluate both the transition behaviour and the steady state behaviour of long fibre MMCs.

Further explanations on the latter behaviour will be provided in subsection 5.2. Here, a physical explanation of the transition behaviour that justifies the method adopted is discussed. Detailed results are only presented for the steady state behaviour whereas the transition behaviour is discussed in a schematic way. This methodology can be applied to different integration points within the structures in order to find the most critical location to assess. Here, for all the geometries considered, the integration point chosen is the one with the highest creep damage.

Fig. 7 shows the schematic transition behaviour for the 3 cross-sections studied for different mechanical loads and dwell times. Contours of the creep strain increment at the stabilised cycle $\Delta\bar{\varepsilon}_{cr_{P4}}$ show the area where the highest creep damage occurs. As discussed in section 3, the load points investigated experience shakedown for both the circular cross-section and the elliptical cross-section if no creep dwell is introduced. Instead reverse plasticity behaviour is expected for the square cross-section. By introducing a creep dwell within the cyclic thermal loading at the tensile peak, different scenarios arise as reported in (Barbera et al., 2016b) for metallic structures at elevated temperature. Here a new mechanism is seen when the off-axis constant mechanical load in Fig. 4-b, is applied. Indeed, for small creep dwell e.g. D1 and no mechanical load M0, the composite with the circular cross-section remains in shakedown while for D100 it experiences a reverse closed loop (RCL). These two material responses have already been discussed in (Barbera et al., 2016b). By increasing the mechanical load e.g. M025, there is a sign variation that leads the structures to experience creep-ratchetting with a total open loop (TOL). This is because the thermal load and the mechanical load act in the opposite direction so that the more the thermal stress relaxes the more the mechanical load becomes predominant. For the highest mechanical load applied, M05, the equivalent stress is positive in loading because the mechanical load is predominant from the first cycle. With regards to the elliptical cross-section, for M0 and all the dwell times, a steady state reverse closed loop response is seen after a transition phase where a sequence of

reverse loops show creep-ratchetting. Compared to the circular cross-section, the reverse closed loops of the elliptical cross-section have the stresses of the loading and creep phases positive from the first cycle (Table 5) to the stabilised one. This is mainly due to the positive value of the stress component along the y direction as it affects the magnitude of the maximum principal component σ_1 such that it becomes predominant during the loading compared to the minimum principal component σ_3. Instead for the circular cross-section the magnitude of the minimum principal component σ_3 is affected by the stress component along the fibre direction z. Therefore the magnitude of σ_3 is higher than σ_1 during loading and lower than σ_1 during unloading. Regarding the square cross-section the creep dwell leads the structure to experience negative reverse ratchetting after a transition phase where the structure experiences positive ratchetting with a reverse open loop. This because the stress relaxation enhances the plastic strain in unloading which after a certain number of cycles is not more compensated by the inelastic strain in loading.

5.2. Steady-state behaviour

The steady-state cyclic stress-strain hysteresis loops for the three geometries studied are presented. Full inelastic step-by-step simulations have been used to verify the LMM results. Modified strain range partitioning, described in section 4, has been used. All the strain increments, ratchetting strains per cycles, and percentage errors are reported in tabular form in order to facilitate the understanding of the method adopted.

Table 6 reports for the circular cross-section the stress and strain ranges computed by the LMM and SBS for the three different load points A1, A2, and A3 in Fig. 4-a and for a dwell time of 100 h. Comparing the results of both approaches, it can be seen that the LMM overestimates the plastic strain range in unloading $\Delta\bar{\varepsilon}_{plP6}$ and the creep strain range $\Delta\bar{\varepsilon}_{crP4}$ for M0. Instead for M025 and M05 the highest percentage error is lower than 16%. The correlation between the ratchetting percentage errors and the type of hysteresis loop for the circular cross-section is shown in Table 7. All the data are computing according to equations (16)–(20). What can be clearly seen in Table 7 is that for M0, a closed reverse loop is considered as $\Delta\bar{\varepsilon}_{rtch} \cong 0$. When the mechanical load increases e.g. M025 or M05, a total open loop is seen as $err\%_{diff}$ is higher than $err\%_{sum}$.

Fig. 8 shows all the stabilised hysteresis loops for the circular cross-section for all the load scenarios investigated. As we have seen in Fig. 7 with regard to the circular cross-section, when the mechanical load is equal zero, there is no sign variation during the stress relaxation and the structure exhibits either shakedown for small dwell times i.e. D1 or reverse plasticity for longer dwell time i.e. D10 and D100. When the off-axis mechanical load is applied the stabilised loop is a total open and creep-ratchetting occurs.

Table 8 compares the stress and strain ranges between LMM and SBS with regards to the elliptical cross-section at D100. Here the LMM overestimates the creep strain range when the mechanical load is M05. For all the other ranges the percentage error is lower than 13%. Table 9, provides the intercorrelations between the percentage errors and the type of hysteresis loop for the elliptical cross-section. As previously discussed for the circular cross-section, when the mechanical load is equal to zero, a closed reverse loop is considered. Instead, creep-ratchetting is seen in the form of total open loop for M025 and M05.

Table 7
Circular cross-section's percentage error for the stabilised hysteresis loops for D100.

	$\Delta\bar{\varepsilon}_{rtch}$	$\Delta\bar{\varepsilon}^{summ}_{rtch}$	$\Delta\bar{\varepsilon}^{diff}_{rtch}$	$err\%_{sum}$	$err\%_{diff}$	M	Loop
LMM	3.00E-6	4.90E-05	3.00E-06	1533.33%	0.00%	M0	RCL
SBS	8.00E-7	3.50E-05	8.00E-07	4275.00%	0.00%		RCL
LMM	6.84E-04	8.16E-04	4.60E-04	19.30%	32.75%	M025	TOL
SBS	6.73E-04	8.14E-04	4.50E-04	20.95%	33.14%		TOL
LMM	7.35E-03	8.00E-03	4.34E-03	6.24%	42.36%	M05	TOL
SBS	7.14E-03	8.06E-03	3.70E-03	12.89%	48.18%		TOL

With regard to the stabilised hysteresis loops for the elliptical cross-section shown in Fig. 9 for all the dwell times investigated the structure's response is in agreement with the results provided in Table 9. For M05, the main difference between the elliptical cross-section and the circular cross-section is that the open loops for the former accumulate plastic strain in loading and unloading. This leads the structure to experience a higher ratchetting strain per cycle compared to the scenario with M025.

Table 10 reports the stress and strain ranges at D100 for the square cross-section for the three load scenarios considered. Here the comparison between LMM and SBS shows a percentage error for all the strain ranges lower than 3%. Table 11 shows the same information as the previous cross-sections investigated reported in Tables 7 and 9. Here reverse open loops are considered for all the load scenarios as $err\%_{diff}$ is always lower than $err\%_{sum}$.

Fig. 10 shows the stabilised hysteresis loops for the square cross-section for all the mechanical loads and dwell times. As we have seen in Fig. 7 the square cross-section shows a reverse ratchetting at the stabilised loop after a certain number of cycles during the transition phase. This is because during the transition phase the sum of the plastic strain in loading $\Delta\varepsilon^{L}_{pl}$ and the creep strain $\Delta\varepsilon_{cr}$ is higher than the plastic strain in unloading $\Delta\varepsilon^{U}_{pl}$. Therefore the loop moves rightward until $\Delta\varepsilon^{U}_{pl}$ is lower than the aforementioned sum. When $\Delta\varepsilon^{U}_{pl}$ becomes dominant the steady-state cycle moves leftward. From Fig. 10 it is clear that the higher the dwell time the sooner the transition from the rightward ratchetting to a leftward ratchetting is reached.

6. Creep fatigue and creep ratchetting assessment

The assessment of the microstructures has been done by considering the effect of the steady-state on the crack initiation process. As depicted in Fig. 7, by changing the applied load and fibre geometry the steady-state response can change remarkably. The scope of this section is to understand and provide more information on how these responses could trigger crack initiation within the metal matrix. It worth noting that the matrix and the fibre are considered perfectly bonded.

6.1. Cyclic thermal load without transverse mechanical load

When no mechanical load is applied, only the thermal stress caused by the coefficient of thermal expansion mismatch is present. For this

Table 6
Circular cross-section stress and strain ranges for the stabilised hysteresis loops for D100.

	$\bar{\sigma}_{eP3}$	$\bar{\sigma}_{eP4}$	$\bar{\sigma}_{eP6}$	$\Delta\bar{\varepsilon}_{plP3}$	$\Delta\bar{\varepsilon}_{crP4}$	$\Delta\bar{\varepsilon}_{plP6}$	$\Delta\bar{\varepsilon}_{rtch}$	
LMM	52.4787	50.858	371	0.00E + 00	2.60E-05	2.30E-05	3.00E-6	M0
SBS	46.089	45.074	371	0.00E + 00	1.71E-05	1.79E-05	8.00E-7	
LMM	138.516	134.053	371	0.00E + 00	6.38E-04	1.78E-04	6.84E-04	M025
SBS	138.694	133.922	371	0.00E + 00	6.32E-04	1.82E-04	6.73E-04	
LMM	291.982	252.392	371	0.00E + 00	6.17E-03	1.83E-03	7.35E-03	M05
SBS	296.096	249.94	371	0.00E + 00	5.88E-03	2.18E-03	7.14E-03	

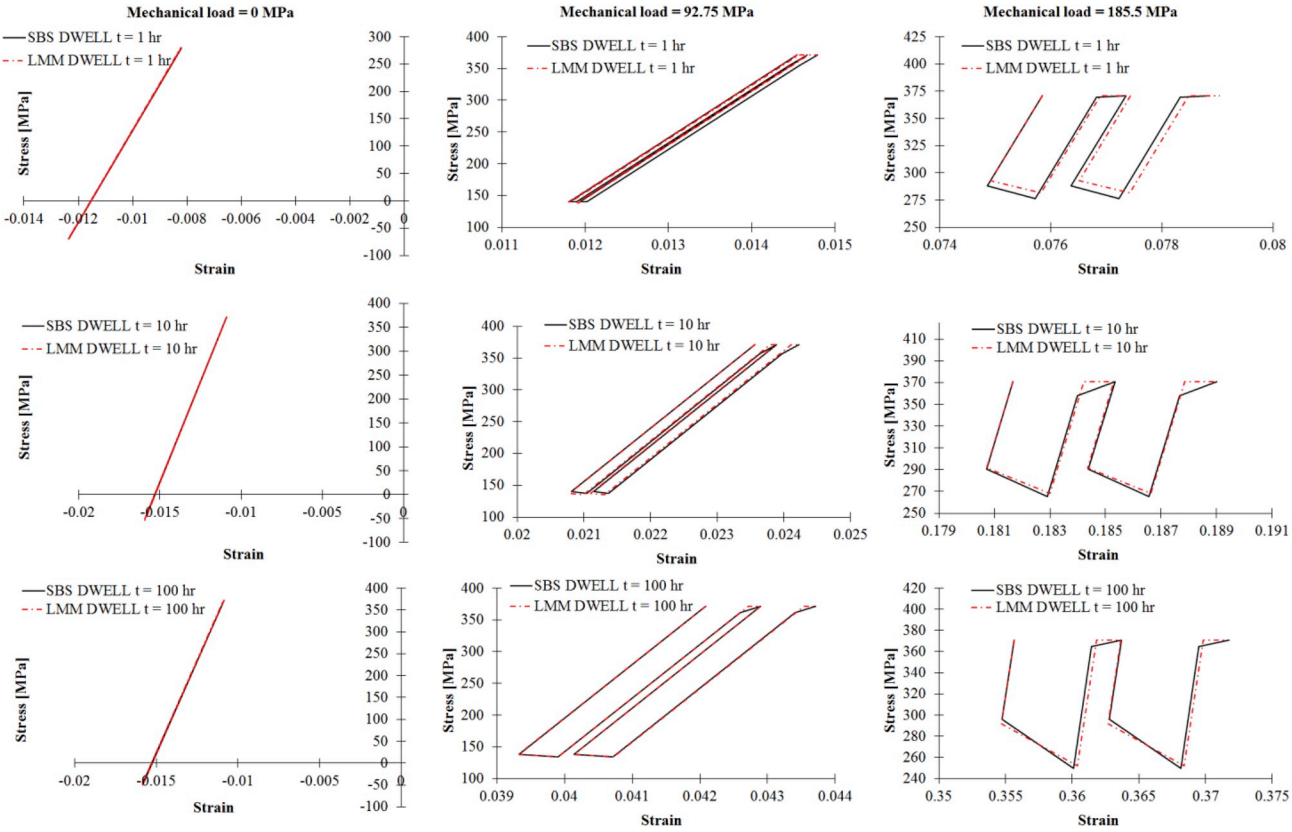

Fig. 8. Steady-state hysteresis loops for the circular cross-section for three dwell times (1hr, 10hrs, 100hrs) and three mechanical load ($\sigma_p = 0$, $\sigma_p = 0.25 \times \sigma_y^{(25)}$, $\sigma_p = 0.5 \times \sigma_y^{(25)}$).

condition, the best geometry is the circular one, as the response is strict shakedown for small dwell times i.e. D1 and closed loop for longer dwell times i.e. D10 and D100 as shown in Fig. 8. For the ellipse and the square section, a closed reverse loop response has been observed for all the dwell times investigated as shown in Figs. 9 and 10. In both cases the creep-fatigue interaction lead to the initiation of a crack within the matrix and it is driven by the creep damage. In both the geometries, the thermal stresses are subjected to a large stress relaxation as shown in Fig. 11a. The stress relaxation is responsible for the creep damage accumulated during each creep dwell. The trend of the stress relaxation is very similar but the stress at the start of the creep dwell is much higher for the square fibre. In turn, as depicted in Fig. 11b, the creep strain accumulated during the increasing creep dwell is larger for the square geometry. This is caused by the higher stress occurring during the creep dwell. The large creep strain accumulation and stress relaxation exhibited by the square fibre is the main cause of reversed creep ratchetting shown in Fig. 7. However, this ratchet strain per cycle is small and compressive preventing any fracture due to excessive deformation.

In terms of overall creep fatigue life, which in both cases is dominated by the creep damage, the ellipse performs generally better than the square fibre as reported in Fig. 12. This is due to the higher stress at the start of the creep dwell of the square fibre, which is 322 MPa against the 226 MPa of the elliptic fibre. For increasing dwell time the endurances predicted for both the geometries reduce significantly. The decrease in creep-fatigue life is nearly linear for the geometries investigated suggesting that both are affected in a similar way by the creep dwell length.

The failure mechanism associated to the cyclic thermal load for a creep dwell of 100 h is depicted in Fig. 13 for both cases. The ellipse has expected life of 36 cycles and the area where the damage initiate is

Table 9
Elliptical cross-section's percentage error for the stabilised hysteresis loops for D100.

	$\Delta\bar{\varepsilon}_{rtch}$	$\Delta\bar{\varepsilon}_{rtch}^{summ}$	$\Delta\bar{\varepsilon}_{rtch}^{diff}$	$err\%_{sum}$	$err\%_{diff}$	M	Loop
LMM	2.00E-5	3.10E-03	2.00E-5	154000.00%	0.00%	M0	RCL
SBS	1.00E-5	3.11E-03	1.00E-5	31000.00%	0.00%		RCL
LMM	4.66E-03	5.51E-03	5.10E-04	18.24%	89.06%	M025	TOL
SBS	4.61E-03	5.78E-03	1.14E-03	25.38%	75.27%		TOL
LMM	5.54E-02	5.67E-03	3.85E-02	2.33%	30.49%	M05	TOL
SBS	5.33E-02	5.75E-03	4.25E-02	7.80%	20.19%		TOL

Table 8
Elliptical cross-section stress and strain ranges for the stabilised hysteresis loops for D100.

	$\bar{\sigma}_{eP3}$	$\bar{\sigma}_{eP4}$	$\bar{\sigma}_{eP6}$	$\Delta\bar{\varepsilon}_{plP3}$	$\Delta\bar{\varepsilon}_{crP4}$	$\Delta\bar{\varepsilon}_{plP6}$	$\Delta\bar{\varepsilon}_{rtch}$	
LMM	226.949	142.733	371	0.00E+00	1.54E-03	1.56E-03	2.00E-5	M0
SBS	228.033	141.01	371	0.00E+00	1.56E-03	1.55E-03	1.00E-5	
LMM	243.826	176.375	371	0.00E+00	2.50E-03	3.01E-03	4.66E-03	M025
SBS	247.21	170.436	371	0.00E+00	2.32E-03	3.46E-03	4.61E-03	
LMM	322.127	267.454	371	1.14E-03	7.95E-03	4.76E-02	5.54E-02	M05
SBS	322	256.712	371	1.25E-03	6.21E-03	5.00E-02	5.33E-02	

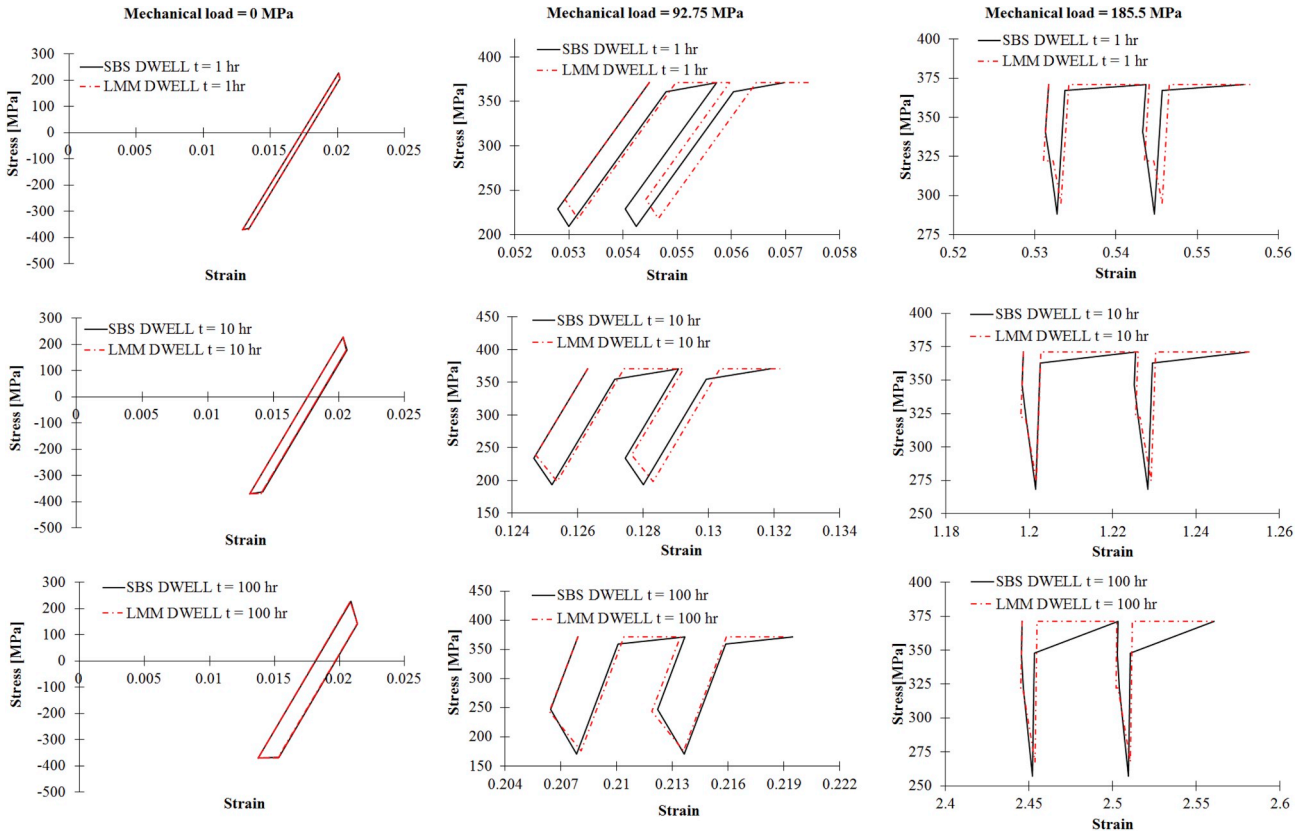

Fig. 9. Steady-state hysteresis loops for the elliptical cross-section for three dwell times (1hr, 10hrs, 100hrs) and three mechanical load ($\sigma_p = 0$, $\sigma_p = 0.25 \times \sigma_y^{(25)}$, $\sigma_p = 0.5 \times \sigma_y^{(25)}$).

Table 10
Square cross-section stress and strain ranges for the stabilised hysteresis loops for D100.

	$\bar{\sigma}_{eP3}$	$\bar{\sigma}_{eP4}$	$\bar{\sigma}_{eP6}$	$\Delta\bar{\varepsilon}_{plP3}$	$\Delta\bar{\varepsilon}_{crP4}$	$\Delta\bar{\varepsilon}_{plP6}$	$\Delta\bar{\varepsilon}_{rtch}$	
LMM	322	185.855	371	2.51E-03	4.17E-03	6.91E-03	2.71E-04	M0
SBS	322	183.691	371	2.51E-03	4.06E-03	6.83E-03	3.00E-04	
LMM	322	185.443	371	2.52E-03	4.06E-03	7.15E-03	5.47E-04	M025
SBS	322	184.072	371	2.47E-03	4.06E-03	7.09E-03	5.02E-04	
LMM	322	198.515	371	2.97E-03	4.69E-03	1.00E-02	2.69E-03	M05
SBS	322	210.653	371	3.01E-03	4.66E-03	1.01E-02	2.65E-03	

Table 11
Square cross-section's percentage error for the stabilised hysteresis loops for D100.

	$\Delta\bar{\varepsilon}_{rtch}$	$\Delta\bar{\varepsilon}_{rtch}^{summ}$	$\Delta\bar{\varepsilon}_{rtch}^{diff}$	$err\%_{sum}$	$err\%_{diff}$	M	Loop
LMM	2.71E-04	1.36E-02	2.30E-04	4914.76%	15.13%	M0	ROL
SBS	3.00E-04	1.34E-02	2.60E-04	4366.67%	13.33%		ROL
LMM	5.47E-04	1.37E-02	5.70E-04	2410.05%	4.20%	M025	ROL
SBS	5.02E-04	1.36E-02	5.60E-04	2613.15%	11.55%		ROL
LMM	2.69E-03	1.77E-02	2.34E-04	556.51%	13.01%	M05	ROL
SBS	2.65E-03	1.78E-02	2.43E-04	570.57%	8.30%		ROL

shown in Fig. 13a. The blue area is relatively large and spread on both fibre sides along the vertical axis. Commonly creep-fatigue failure mechanism is considered a localized mechanism associated to the initiation of a crack, as it is for the square (Fig. 13b). However, for the elliptical cross section a remarkable volume of material is expected to fail. This can be explained by considering the effect of the fibre geometry, which enhances the geometrical constraint between each fibre. Conversely, for the square the failure mechanism is localized at the inner edge of the square fibre, where the stresses are at the highest point. This causes a significant reduction in creep-fatigue life, which for the case considered is only 3 cycles.

6.2. Cyclic thermal load with a transverse mechanical load

When a mechanical load is applied, all the geometries analysed tend to exhibit creep ratchetting, which competes with creep-fatigue crack initiation. The increase of dwell time enhances the creep and fatigue damage in all the geometries. Also, creep-ratchetting is affected by the dwell time considered and the magnitude of inelastic strain accumulated at each cycle also increases with the mechanical load. When a constant transverse mechanical of 92.75 MPa is applied, creep-fatigue interaction and creep-ratchetting compete. For circular and elliptical cross-section, Fig. 14a and b, creep-fatigue interaction is dominant up to a threshold. This threshold is dependent on the cross-section and is around 30 h and 10 h for the circular and elliptical cross-section respectively. Creep-ratchetting becomes a significant failure mechanism only for long dwells, leading to a high-temperature fracture within the matrix. Conversely for the square cross-section, as it is shown in Fig. 14c, creep-fatigue interaction is always dominant.

The cyclic stress response obtained for the three geometries at each loading step is reported in Fig. 15, where the von Mises stress contours for a cyclic temperature of 175 °C and a constant mechanical load of 92.75 MPa are shown. The stress distribution at each loading step is dramatically affected by the fibre's shape. During the loading, phase increasing stress levels can be observed, the highest is obtained by the square fibre. The subsequent creep dwell induces a stress relaxation, which leads to partial stress redistribution. This is evident for the elliptical cross-section, which shows a clear change of the most stressed location. Conversely for the circular fibre, stress relaxation is marginal and no significant stress redistribution occurs. In the square fibre, the

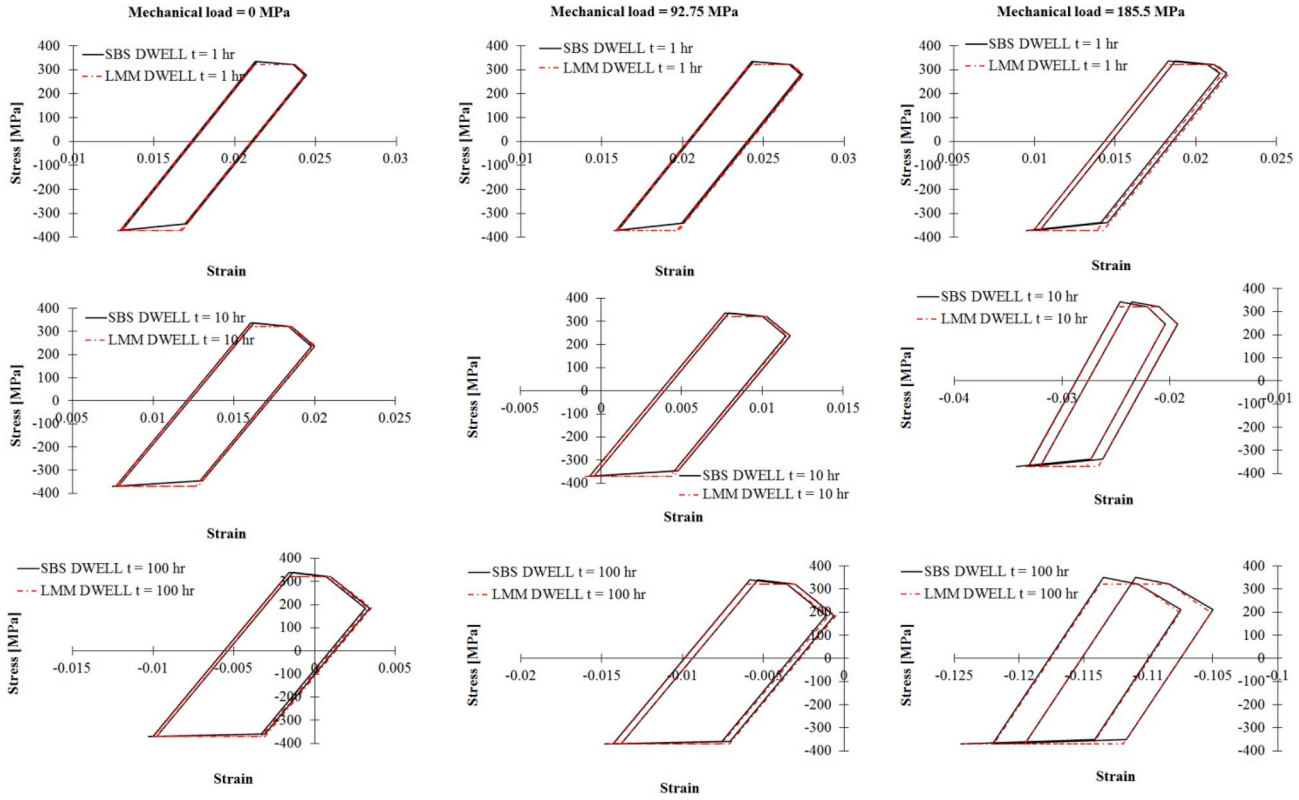

Fig. 10. Steady-state hysteresis loops for the square cross-section for three dwell times (1hr, 10hrs, 100hrs) and three mechanical load ($\sigma_p = 0$, $\sigma_p = 0.25 \times \sigma_y^{(25)}$, $\sigma_p = 0.5 \times \sigma_y^{(25)}$).

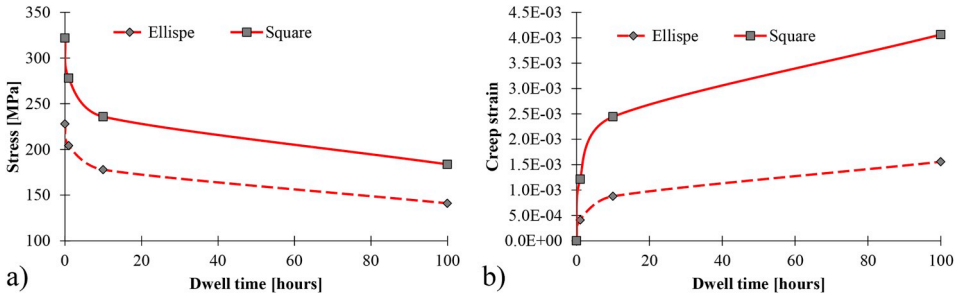

Fig. 11. a) Stress relaxation and b) creep strain accumulation during increasing creep dwell.

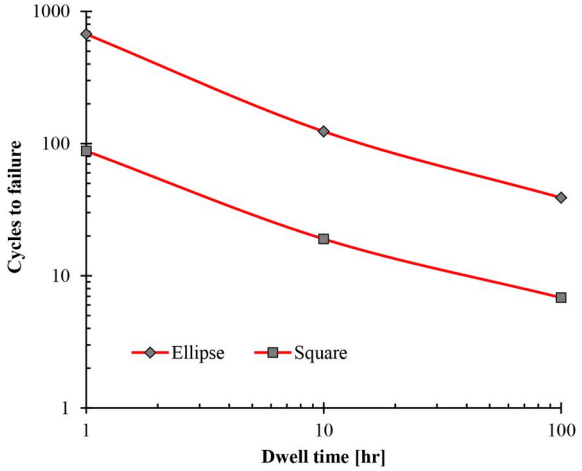

Fig. 12. Creep-fatigue endurances for the ellipse and circle fibres without mechanical load.

large residual stresses generated by cyclic plasticity leads to a large stress relaxation and redistribution. During the unloading phase, all the geometries respond in a similar way reaching the yield in a large area of the matrix.

By considering the results obtained and shown in Fig. 15 and the cyclic responses reported in Figs. 8, Figs. 9 and 10 it is clear that the failure mechanisms are profoundly affected by a series of crucial parameters. These crucial parameters are the stress at the start of the creep dwell, which mainly affects the creep damage and the total strain range that affect the fatigue damage. The stress at the start of the creep dwell has been found to be always tensile and relatively high. The highest stress of 322 MPa has been identified in the square fibre and the lowest of 132 MPa in the circular fibre. For all the cases studied creep damage has consistently been found to be more damaging than fatigue damage, which is never dominant except for very short dwells.

7. Conclusions

In this work, the effect of fibre cross-section geometry i.e. circular, elliptical and square cross section, on the cyclic response of MMCs at high-temperature has been addressed for different load conditions.

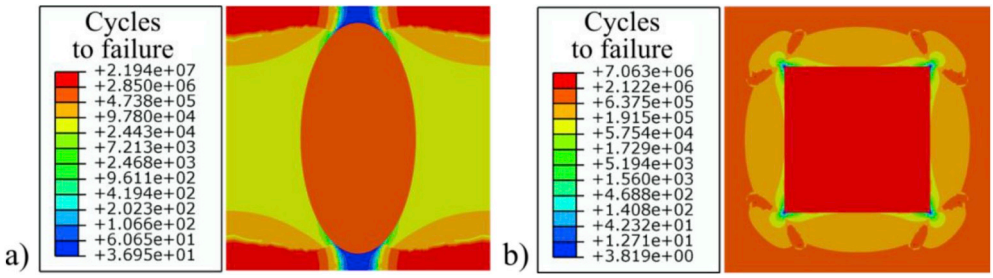

Fig. 13. Creep-fatigue life of the a) ellipse and b) square fibre subjected to a cyclic thermal load and a creep dwell of 100 h.

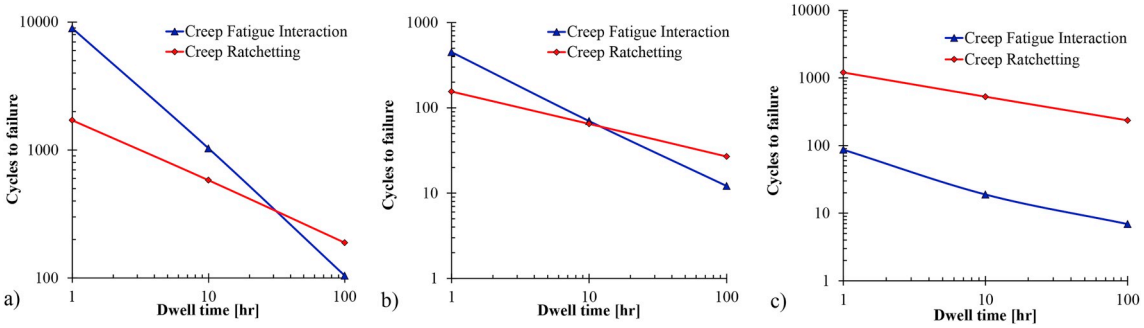

Fig. 14. Creep-fatigue and creep ratchetting endurances for the a) circular, b) elliptical and c) square geometries subjected to cyclic temperature of 175 °C and a constant mechanical load of 92.75 MPa with an increasing dwell time.

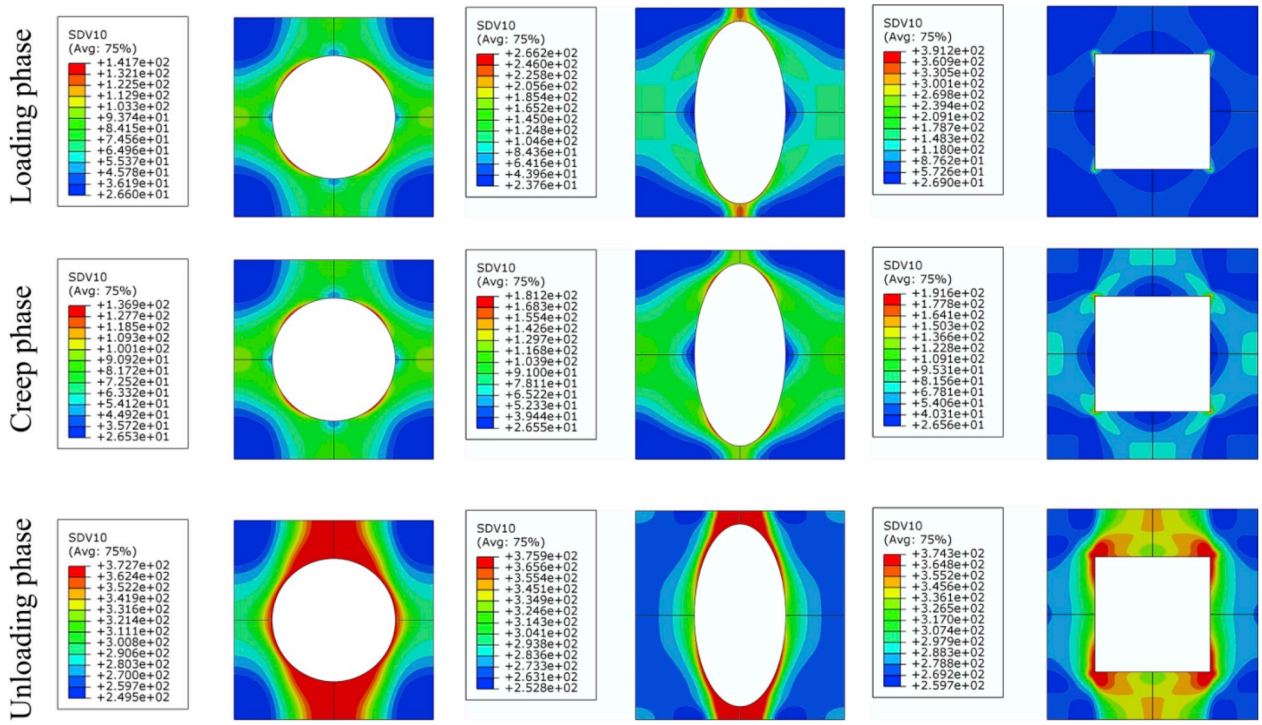

Fig. 15. von Mises stress for circular, elliptical and square cross-sections subjected to cyclic temperature of 175 °C and a constant mechanical load of 92.75 MPa with 100 h of creep dwell time.

The main results obtained within this research work are as follow:

1. Transitional behaviour of the hysteresis loops has been carefully identified and discussed. This has been found to be mainly affected by the local thermomechanical stress. Furthermore, the final response of the stabilised hysteresis loop is drastically influenced by the magnitude of the mechanical load. When this dominates over thermal load, creep ratchetting is observed.
2. In terms of structural integrity, as expected, the circular cross-section is the most reliable. However, when primary load is applied, creep-ratchetting is always present. For the circular and elliptical cross-sections ratchetting becomes dominant by a precise threshold. Conversely, creep-fatigue interaction is dominant for the square cross-section.

3. For all the geometries and load conditions examined the most critical damage mechanism is the high-temperature creep, which dominates over the fatigue damage. This is enhanced mainly by the high level of stress at the start of the creep dwell. The introduction of a creep dwell poses severe limitations to the material endurance that needs to be accounted during the design process.
4. Both shapes of the fibre cross-section and fibre arrangement can be detrimental regarding the creep-fatigue life by enhancing the geometrical constraint. This has been identified for the elliptical cross-section, where the creep-fatigue crack initiation tends to initiate in a larger area compared to the other two geometries.

With regards to the numerical procedure employed, a modification of the existing strain range partitioning procedure for the treatment of multiaxial creep-fatigue has been proposed which is based on basic rules to construct the proper stabilised hysteresis loop. These rules have been crucial for an accurate assessment of the microstructural integrity for different loading conditions. In addition, a detailed procedure to evaluate the sign of von Mises stress, at the stabilised hysteresis loop, has been reported. It relies upon the comparison between the ratchetting strains in equations (16)–(18). Besides, the LMM with its eDSCA numerical method has been used along with incremental FEA for all the simulations of this study. The possibility to investigate composites in the microscale by means of the LMM relies upon its capability to employ multilaterals (matrix and fibre material properties can be assigned separately) for all types of simulations it can perform.

In conclusion, all the numerical results found, further extended the knowledge of the creep-fatigue interaction response of MMCs subjected to cyclic load at high-temperature. The information obtained forms the basis necessary to construct a macro-scale model for the creep-fatigue response, which is currently unavailable. Furthermore, the extensively validation carried out by means of inelastic step-by-step finite element analysis demonstrates the capabilities of direct methods, such as the LMM, to provide feasible results with a lower computational cost.

Data availability

The raw data required to reproduce these findings are available to download from https://doi.org/10.15129/13787d1c-1741-4445-a042-b33e021ba8e5.

Acknowledgement

The authors gratefully acknowledge the support of the University of Strathclyde, the Royal Society (IE140842), the International Cooperation and Exchange Project NSFC (11511130057) and the National Science Foundation for Distinguished Young Scholars of China (11325211) during the course of this work.

Appendix A. Supplementary data

Supplementary data to this article can be found online at https://doi.org/10.1016/j.euromechsol.2018.10.015.

References

Abaqus, C., 2013. Software for Finite Element Analysis Abaqus/Complete Abaqus Environment, Version 6.12. Dassault Systémes. Vélizy-Villacoublay.
Aboudi, J., Arnold, S.M., Bednarcyk, B.A., 2012. Micromechanics of Composite Materials: a Generalized Multiscale Analysis Approach. Butterworth-Heinemann.
Barbera, D., Chen, H., Liu, Y., 2016a. Creep-fatigue behaviour of aluminum alloy-based metal matrix composite. Int. J. Pres. Ves. Pip. 139–140, 159–172.
Barbera, D., Chen, H., Liu, Y., 2016b. On Creep Fatigue interaction of components at elevated temperature. J. Pressure Vessel Technol. 138 041403.
Bettge, D., Günther, B., Wedell, W., Portella, P.D., Hemptenmacher, J., Peters, P., Skrotzki, B., 2007. Mechanical behavior and fatigue damage of a titanium matrix composite reinforced with continuous SiC fibers. Mater. Sci. Eng., A 452, 536–544.
Bree, J., 1967. Elastic-plastic behaviour of thin tubes subjected to internal pressure and intermittent high-heat fluxes with application to fast-nuclear-reactor fuel elements. J. Strain Anal. 2, 226–238.
Cantor, B., Dunne, F.P., Stone, I.C., 2003. Metal and Ceramic Matrix Composites. CRC Press.
Chen, H., 2010. Lower and upper bound shakedown analysis of structures with temperature-dependent yield stress. J. Pressure Vessel Technol. 132 011202.
Chen, H., Chen, W., Ure, J., 2014. A direct method on the evaluation of cyclic steady state of structures with creep effect. J. Pressure Vessel Technol. 136, 061404.
Chen, H., Ponter, A.R., 2005. On the behaviour of a particulate metal matrix composite subjected to cyclic temperature and constant stress. Comput. Mater. Sci. 34, 425–441.
Chen, H., Ponter, A.R., 2006. Linear Matching Method on the evaluation of plastic and creep behaviours for bodies subjected to cyclic thermal and mechanical loading. Int. J. Numer. Methods Eng. 68, 13–32.
Chen, H., Ponter, A.R., 2010. A direct method on the evaluation of ratchet limit. J. Pressure Vessel Technol. 132 041202.
Chen, M., Hachemi, A., 2014. Progress in Plastic Design of Composites, Direct Methods for Limit States in Structures and Materials. Springer, pp. 119–138.
Coffin Jr., L., 1954. A study on the effects of cyclic thermal stress on a ductile metal. Trans. ASME 76.
Daehn, G., Zhang, H., Chen, Y.-C., 1991. Approaches to modeling the plastic deformation of metal matrix composites under thermal cycling conditions. Modeling the deformation of crystalline solids 665–678.
Doghri, I., Adam, L., Bilger, N., 2010. Mean-field homogenization of elasto-viscoplastic composites based on a general incrementally affine linearization method. Int. J. Plast. 26, 219–238.
EDF Energy, 2014. Assessment Procedure for the High Temperature Response of Structures. R5 Issue 3.
Giugliano, D., Barbera, D., Chen, H., 2017. Effect of fiber cross section geometry on cyclic plastic behavior of continuous fiber reinforced aluminum matrix composites. Eur. J. Mech. Solid. 61, 35–46.
Giugliano, D., Chen, H., 2016. Micromechanical modeling on cyclic plastic behavior of unidirectional fiber reinforced aluminum matrix composites. Eur. J. Mech. Solid. 59, 155–164.
Gorash, Y., Chen, H., 2013. Creep-fatigue life assessment of cruciform weldments using the linear matching method. Int. J. Pres. Ves. Pip. 104, 1–13.
Guo, S., Kang, G., Zhang, J., 2011. Meso-mechanical constitutive model for ratchetting of particle-reinforced metal matrix composites. Int. J. Plast. 27, 1896–1915.
Guo, S., Kang, G., Zhang, J., 2013. A cyclic visco-plastic constitutive model for time-dependent ratchetting of particle-reinforced metal matrix composites. Int. J. Plast. 40, 101–125.
Guo, S.J., Kang, G.Z., Dong, C., 2007. Numerical simulations for uniaxial ratcheting of SiCp/6061Al composites concerning particulate arrangement. Advanced Materials Research. Trans Tech Publ 317–320.
Hales, R., 1980. A quantitative metallographic assessment of structural degradation of type 316 stainless steel during creep-fatigue. Fatig. Fract. Eng. Mater. Struct. 3, 339–356.
Hales, R., Holdsworth, S., O'Donnell, M., Perrin, I., Skelton, R., 2002. A code of practice for the determination of cyclic stress-strain data. Mater. A. T. High. Temp. 19, 165–185.
Halford, G.R., Lerch, B.A., Arya, V.K., 2000. Thermal Strain Fatigue Modeling of a Matrix Alloy for a Metal Matrix Composite, Thermo-mechanical Fatigue Behavior of Materials: Third Volume. ASTM International.
Hertz-Clemens, S., Aumont, C., Rémy, L., 2002. Damage mechanisms under thermal-Mechanical fatigue in a unidirectionally reinforced SiC-titanium metal matrix composite for advanced jet engine components. European Structural Integrity Society 29, 125–133.
Jansson, S., Dal Bello, D., Leckie, F., 1994. Transverse and cyclic thermal loading of the fiber reinforced metal-matrix composite SCS6/Ti-15-3. Acta Metall. Mater. 42, 4015–4024.
Jansson, S., Leckie, F., 1992. Mechanical behavior of a continuous fiber-reinforced aluminum matrix composite subjected to transverse and thermal loading. J. Mech. Phys. Solid. 40, 593–612.
Jansson, S., Leckie, F.A., 1991. Mechanical Behavior of a Continuous Fiber Reinforced Aluminum Matrix Composite Subjected to Transverse and Thermal Loading.
Kang, G., 2004. A visco-plastic constitutive model for ratcheting of cyclically stable materials and its finite element implementation. Mech. Mater. 36, 299–312.
Kang, G., 2006. Uniaxial time-dependent ratchetting of SiCP/6061Al composites at room and high temperature. Compos. Sci. Technol. 66, 1418–1430.
Kang, G., 2008. Ratchetting: recent progresses in phenomenon observation, constitutive modeling and application. Int. J. Fatig. 30, 1448–1472.
Kang, G., Dong, C., Guo, S., 2007. Finite element analysis for uniaxial time-dependent ratcheting of SiC P/6061Al composites at room and high temperatures. Mater. Sci. Eng., A 458, 170–183.
Karakaş, Ö., Szusta, J., 2015. Monotonic and low cycle fatigue behaviour of 2024-T3 aluminium alloy between room temperature and 300 °C for designing VAWT components. Fatig. Fract. Eng. Mater. Struct.
Manson, S., 1965. Fatigue: a complex subject—some simple approximations. Exp. Mech. 5, 193–226.
Manson, S., Halford, G., 1976. Treatment of Multiaxial Creep-fatigue by Strainrange Partitioning.
Manson, S.S., 1954. Behavior of Materials under Conditions of Thermal Stress. NACA.
Manson, S.S., 1968. A simple procedure for estimating high-temperature low-cycle fatigue. Exp. Mech. 8, 349–355.
Maximov, J., Duncheva, G., Anchev, A., Ichkova, M., 2014. Modeling of strain hardening and creep behaviour of 2024T3 aluminium alloy at room and high temperatures. Comput. Mater. Sci. 83, 381–393.

Mirdamadi, M., Johnson, W.S., 1996. Modeling and Life Prediction Methodology for Titanium Matrix Composites Subjected to Mission Profiles, Life Prediction Methodology for Titanium Matrix Composites. ASTM International.
Mondali, M., Abedian, A., Adibnazari, S., 2005. FEM study of the second stage creep behavior of Al6061/SiC metal matrix composite. Comput. Mater. Sci. 34, 140–150.
Muralidharan, U., Manson, S., 1988. A modified universal slopes equation for estimation of fatigue characteristics of metals. J. Eng. Mater. Technol. 110, 55–58.
Nicholas, T., Russ, S.M., Neu, R.W., Schehl, N., 1996. Life Prediction of a [0/90] Metal Matrix Composite under Isothermal and Thermomechanical Fatigue, Life Prediction Methodology for Titanium Matrix Composites. ASTM International.
Plumbridge, W., 1987. Metallography of High Temperature Fatigue. High Temperature Fatigue. Springer, Dordrecht, pp. 177–228.
Ponter, A., Leckie, F., 1998a. Bounding properties of metal-matrix composites subjected to cyclic thermal loading. J. Mech. Phys. Solid. 46, 697–717.
Ponter, A., Leckie, F., 1998b. On the behaviour of metal matrix composites subjected to cyclic thermal loading. J. Mech. Phys. Solid. 46, 2183–2199.
Rutecka, A., Kowalewski, Z.L., Pietrzak, K., Dietrich, L., Makowska, K., Woźniak, J., Kostecki, M., Bochniak, W., Olszyna, A., 2011. Damage development of Al/SiC metal matrix composite under fatigue, creep and monotonic loading conditions. Procedia Engineering 10, 1420–1425.
Shao, X., Kang, G., Guo, S., 2009. 3D finite element analysis for time-dependent ratcheting of SiC_P/6061Al composites considering interface bonding. Acta Mater. Compos. Sin. 2, 006.
Shao, X., Kang, G., Guo, S., Zhang, J., 2010. Finite element analysis for effects of stochastic properties of particles on ratcheting of SiC_P/6061Al composites. Acta Mater. Compos. Sin. 3 020.
Skelton, R., Maier, H., Christ, H.-J., 1997. The Bauschinger effect, Masing model and the Ramberg–Osgood relation for cyclic deformation in metals. Mater. Sci. Eng., A 238, 377–390.
Wada, Y., Aoto, K., Ueno, F., 1997. Creep-fatigue Evaluation Method for Type 304 and 316FR SS.
Xuanchen Zhu, H.C., Xuan, Fuzhen, Chen, Xiaohui, 2017. Cyclic plasticity behaviors of steam turbine rotor subjected to cyclic thermal and mechanical loads. Eur. J. Mech. Solid. 66, 243–255.
Zhang, H., Daehn, G.S., Wagoner, R., 1990. The temperature-cycling deformation of particle reinforced metal matrix composites—a finite element study. Scripta Metall. Mater. 24, 2151–2155.